

N. Mihajlović

e-mail: N.Mihajlovic@tue.nl

A. A. van Veggel

e-mail: A.A.v.Veggel@tue.nl

N. van de Wouw

e-mail: N.v.d.Wouw@tue.nl

H. Nijmeijer

e-mail: H.Nijmeijer@tue.nl

Eindhoven University of Technology, Department
of Mechanical Engineering, Dynamics and
Control Group, Den Dolech, PO Box 513, 5600
MB Eindhoven, The Netherlands

Analysis of Friction-Induced Limit Cycling in an Experimental Drill-String System

In this paper, we aim for an improved understanding of the causes for torsional vibrations that appear in rotary drilling systems used for the exploration of oil and gas. For this purpose, an experimental drill-string setup is considered. In that system, torsional vibrations with and without stick-slip are observed in steady state. In order to obtain a predictive model, a discontinuous static friction model is proposed. The steady-state behavior of the drill-string system is analyzed both numerically and experimentally. A comparison of numerical and experimental bifurcation diagrams indicates the predictive quality of the model. Moreover, specific friction model characteristics can be linked to the existence of torsional vibrations with and without stick-slip. [DOI: 10.1115/1.1850535]

1 Introduction

Deep wells for the exploration and production of oil and gas are drilled with a rotary drilling system, which creates a borehole by means of a rock-cutting tool called a bit. The torque driving the bit is generated at the surface by a motor with a mechanical transmission box. Via the transmission, the motor drives the rotary table: a large disk that acts as a kinetic energy storage unit. The medium to transport the energy from the surface to the bit is a drill-string, mainly consisting of drill pipes: slender tubes, about 9 m long, coupled with threaded connections, having a typical outside diameter of 127 mm and a wall thickness of 9 mm [1–5]. However, smaller (e.g., 89 mm) and larger (e.g., 165 mm) drill pipe diameters are also used. The drill-string can be up to 8 km long. The lowest part of the drill-string is the bottom-hole assembly consisting of drill collars and the bit. Dependent on the diameter of the hole, these drill collars have an inner diameter of 64–76 mm and an outer diameter of 120–240 mm. The bottom-hole assembly can be several hundred meters long.

The drill-string undergoes various types of vibrations during drilling [1,3–5]:

- torsional (rotational) vibrations, caused by nonlinear interaction between the bit and the rock or the drill-string and the borehole wall. The frequency of the vibrations is usually somewhat below the first natural frequency of torsional vibrations, i.e., of the order of 0.05–0.5 Hz [1,2].
- bending (lateral) vibrations, often caused by pipe eccentricity, leading to centripetal forces during rotation
- axial (longitudinal) vibrations, due to bouncing of the drilling bit on the rock during rotation
- hydraulic vibrations in the circulation system, stemming from pump pulsations

Drill-string vibrations are an important cause for premature failure of drill-string components and drilling inefficiency. In this paper, torsional drill-string vibrations are investigated. Since the behavior of the system when a constant torque is applied at the rotary table of a drill-string system is of interest, the focus is on the steady-state behavior of drill-string systems for such constant torques.

Extensive research on the subject of torsional vibrations has already been conducted [1–9]. According to some of those results,

the cause for torsional vibrations is the stick-slip phenomenon due to the friction force between the bit and the well [1–5]. Moreover, the cause for torsional vibrations can be the negative damping in the friction force present due to the contact between the bit and the borehole (see, for example, [6,7]). In order to gain an improved understanding of the causes for torsional vibrations, an experimental drill-string setup is built. The setup consists of a DC-motor that is connected to the upper disk via a gear box. The upper and lower disks are connected via a low stiffness string and, at the lower disk, an additional brake is applied. In the setup, torsional vibrations with and without stick-slip are observed and the behavior of the setup is analyzed. However, using existing friction models, which are used for modeling torsional vibrations in drill-string systems [1–5,7], not all steady-state phenomena observed in the experimental drill-string system can be modeled. Using another discontinuous static friction model, those experimentally observed phenomena are successfully predicted. In such a friction model, positive damping is present for very small angular velocities; for higher angular velocities, negative damping occurs, and for even higher angular velocities, positive damping is again present in the friction (see [10–14]). In [10,11], such a friction model is called a “humped friction model.” It follows that both in the model and the experiments the steady-state performance undergoes various qualitative changes when the input voltage is changed. These qualitative changes are typically captured in a bifurcation diagram that features the changes of equilibrium points into limit cycling (vibrations). A comparison of numerical and experimental bifurcation diagrams illustrates the predictive quality of the suggested model. Moreover, such a bifurcation diagram provides improved insight into how torsional vibrations in drill-string systems are created.

In Sec. 2, the experimental drill-string setup is described. Next, the dynamic behavior of the setup is modeled, the parameters of the model are estimated, and the obtained model is validated. In the experimental system as well as in the estimated model both equilibria (constant velocity) and limit cycles (torsional vibrations) are observed when a constant input torque is applied. Therefore, in Sec. 3, the equilibrium point (set) is determined and related stability properties are discussed. Next, periodic solutions and their stability properties are determined numerically. Subsequently, based on the proposed model and estimated parameters, a bifurcation diagram is presented and compared to experimentally obtained results in Sec. 4. In Sec. 5, conclusions are presented.

2 Drill-String Setup

2.1 Description of Setup. The experimental drill-string setup is shown in Fig. 1. The setup consists of a power amplifier,

Contributed by the Dynamic Systems, Measurement, and Control Division of THE AMERICAN SOCIETY OF MECHANICAL ENGINEERS for publication in the ASME JOURNAL OF DYNAMIC SYSTEMS, MEASUREMENT, AND CONTROL. Manuscript received by the ASME Dynamic Systems and Control Division June 17, 2003; final revision, November 4, 2003. Review conducted by: K. Stelson.

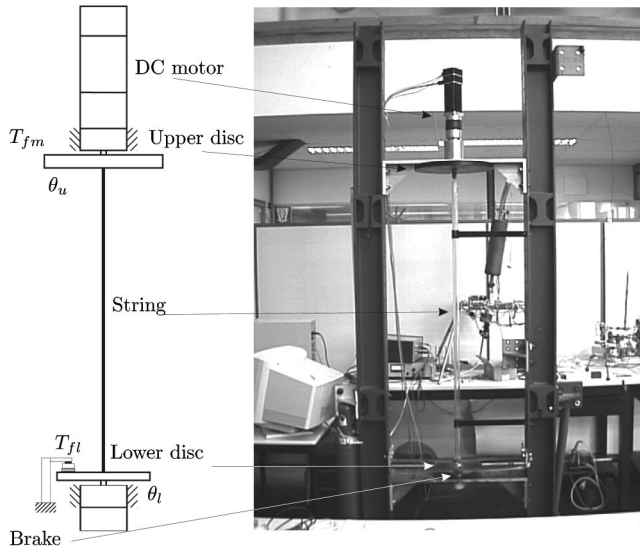


Fig. 1 Experimental drill-string setup

a DC motor, two rotational disks (upper and lower), a low-stiffness string, and an additional brake applied to the lower disk. The input voltage from the computer, which is between -5 V and 5 V, is fed into the DC motor via the power amplifier. The DC motor, which represents the drive motor of a real drill rig, is connected via the gear box to the upper steel disk (which represents the rotary table of the rig). The upper and lower disks are connected through a low-stiffness steel string. The string is 1.5 m long and the diameter of the string is 2 mm. The drill-string and the lower brass disk represent the drill-string with the bottom-hole assembly at the real drill-rig, and the additional brake implements the friction force between the drill bit and borehole. The contact material of the brake is rubber. The angular positions of the upper and lower disks are measured using incremental encoders. The angular velocities of both disks are obtained by numerical differentiation of the angular positions and filtering the resulting signals using a low-pass filter with a cutoff frequency of 200 rad/s (31.8 Hz). In Fig. 1, as well as further on in the text, θ_u and θ_l are the angular positions of the upper and lower disks, respectively; T_{fm} is the friction torque present at the upper disk; and T_{fl} represents the friction torque at the lower disk.

2.2 Model of the Setup. The drill-string setup is an electro-mechanical system. The model of the motor can be described by

$$au = L_r i_r + (R_i + R_r) i_r + n k_{em} \dot{\theta}_u \quad (1)$$

$$T_m = n k_{me} i_r$$

where u is the input voltage to the power amplifier; a is the amplification factor of the power amplifier; R_i is the output resistance of the amplifier; L_r and R_r are the inductance and the resistance of the rotor circuit, respectively; i_r represents the rotor current; n is reduction ratio of the gear; k_{em} and k_{me} are the electromotive force constant and the torque constant, respectively; and T_m is the motor torque. In (1) and further in the text, a dot above a variable indicates a time derivation (e.g., $i_r = di_r/dt$). The model of the mechanical part of the setup can be described by the following pair of second-order differential equations:

$$J_u \ddot{\theta}_u + b_\theta (\dot{\theta}_u - \dot{\theta}_l) + k_\theta (\theta_u - \theta_l) + T_{fm}(\dot{\theta}_u) = T_m \quad (2)$$

$$J_l \ddot{\theta}_l - b_\theta (\dot{\theta}_u - \dot{\theta}_l) - k_\theta (\theta_u - \theta_l) + T_{fl}(\dot{\theta}_l) = 0$$

with the set-valued friction laws

$$T_{fm}(\dot{\theta}_u) \in \begin{cases} T_{mp}(\dot{\theta}_u) & \text{for } \dot{\theta}_u > 0 \\ [-T_{mn}(0), T_{mp}(0)] & \text{for } \dot{\theta}_u = 0 \\ -T_{mn}(\dot{\theta}_u) & \text{for } \dot{\theta}_u < 0 \end{cases} \quad (3)$$

$$T_{fl}(\dot{\theta}_l) \in \begin{cases} T_{lp}(\dot{\theta}_l) & \text{for } \dot{\theta}_l > 0 \\ [-T_{ln}(0), T_{lp}(0)] & \text{for } \dot{\theta}_l = 0 \\ -T_{ln}(\dot{\theta}_l) & \text{for } \dot{\theta}_l < 0 \end{cases}$$

In (2) J_u and J_l are moments of inertia of the upper and lower disk with respect to the corresponding centers of mass, respectively, and b_θ , k_θ are the torsional damping and the stiffness parameters of the string, respectively. In (2) and (3) T_{fm} represents the friction torque of the motor caused by the friction in the gear box and in the bearings, T_{fl} is the friction torque present at the lower disk which is caused by the friction between lower disk and the brake and the friction in the bearings at the lower disk. Nonlinear functions $T_{mp}(\dot{\theta}_u)$, $T_{mn}(\dot{\theta}_u)$ represent complete friction torques present in the bearings and motor for positive and negative, though nonzero, angular velocities $\dot{\theta}_u$, respectively, and $T_{lp}(\dot{\theta}_l)$ and $T_{ln}(\dot{\theta}_l)$ represent complete friction torques which act on the lower disk for positive and negative, though nonzero, angular velocities $\dot{\theta}_l$ and for those nonlinear functions the following conditions hold:

$$T_{mp}(\dot{\theta}_u), T_{lp}(\dot{\theta}_l) > 0, \forall \dot{\theta}_u, \dot{\theta}_l \geq 0 \quad \text{and} \quad (4)$$

$$T_{mn}(\dot{\theta}_u), T_{ln}(\dot{\theta}_l) > 0, \forall \dot{\theta}_u, \dot{\theta}_l \leq 0$$

which means that the friction torques are dissipative.

Equation (3) reflects that set-valued¹ friction laws are used to model the friction at the upper and lower disc. The reason for this choice is the fact that both at the upper and at the lower disc the sticking phenomenon is observed.

From (3), it can be noted that the friction torques are modeled using a static friction model. This choice is based on the following reasoning: we are interested in the steady-state behavior of the setup and not in the detailed dynamic modeling of the friction for very small angular velocities.

In the sequel, the following assumptions are adopted:

- $L_r = 0$: Since the electrical part of the system has much faster dynamics than the mechanical part, the inductance of the rotor circuit is neglected. Moreover, with this assumption the model of the setup is of a lower order.
- $k_{me} = k_{em}$: This is valid only when there is no loss of energy in the magnetic field of the DC motor (for more information see [15]). This loss of energy is expected to be very small.
- $b_0 = 0$: The torsional damping of the string is very small compared to the damping effects in the bearings and is therefore neglected.

If we combine these assumptions with (1) and (2), then the following model of the setup can be obtained:

$$J_u \ddot{\theta}_u + k_\theta (\theta_u - \theta_l) + \left[\frac{n^2 k_{em} k_{me}}{R_i + R_r} \dot{\theta}_u + T_{fm}(\dot{\theta}_u) \right] = \frac{a n k_{me}}{R_i + R_r} u \quad (5)$$

$$J_l \ddot{\theta}_l - k_\theta (\theta_u - \theta_l) + T_{fl}(\dot{\theta}_l) = 0$$

Next, by introduction of $T_{fu}(\dot{\theta}_u)$ as

$$T_{fu}(\dot{\theta}_u) = \frac{n^2 k_{em} k_{me}}{R_i + R_r} \dot{\theta}_u + T_{fm}(\dot{\theta}_u) \quad (6)$$

and k_m as

¹With the set $[a, b]$ we mean the interval $\{x \in \mathbb{R} | a \leq x \leq b\}$.

$$k_m = \frac{ank_{me}}{R_i + R_r} \quad (7)$$

the following model of the drill-string system can be obtained:

$$\begin{aligned} J_u \ddot{\theta}_u + k_\theta(\theta_u - \theta_l) + T_{fu}(\dot{\theta}_u) &= k_m u \\ J_l \ddot{\theta}_l - k_\theta(\theta_u - \theta_l) + T_{fl}(\dot{\theta}_l) &= 0 \end{aligned} \quad (8)$$

where $T_{fu}(\dot{\theta}_u)$ represents the equivalent friction torque present at the upper disk and k_m represents the motor constant. From (6), it can be concluded that $T_{fu}(\dot{\theta}_u)$ consists of the bearing friction torque $T_{fm}(\dot{\theta}_u)$ at the upper disk and the additional term $(n^2 k_{em} k_{me}) \dot{\theta}_u / (R_i + R_r)$, which has the nature of a viscous friction and is due to the electromagnetic characteristics of the DC motor.

According to (3) and (6), T_{fu} can be characterized as follows:

$$T_{fu}(\dot{\theta}_u) \in \begin{cases} T_{up}(\dot{\theta}_u) & \text{for } \dot{\theta}_u > 0 \\ [-T_{un}(0), T_{up}(0)] & \text{for } \dot{\theta}_u = 0 \\ -T_{un}(\dot{\theta}_u) & \text{for } \dot{\theta}_u < 0 \end{cases} \quad (9)$$

where T_{up} and $-T_{un}$ represent the equivalent friction torque present at the upper disk for positive and negative nonzero angular velocities, with $T_{up}(0) = T_{mp}(0)$ and $T_{un}(0) = T_{mn}(0)$. The dynamics of the fourth-order system (8), can be described by a third-order state-space system because its dynamics is independent of the angular positions of the disks, but depends on the difference between these two angular positions. Therefore, by choosing state coordinates defined by $x_1 = \theta_u - \theta_l$, $x_2 = \dot{\theta}_u$ and $x_3 = \dot{\theta}_l$, the following state-space model can be obtained:

$$\dot{x}_1 = x_2 - x_3$$

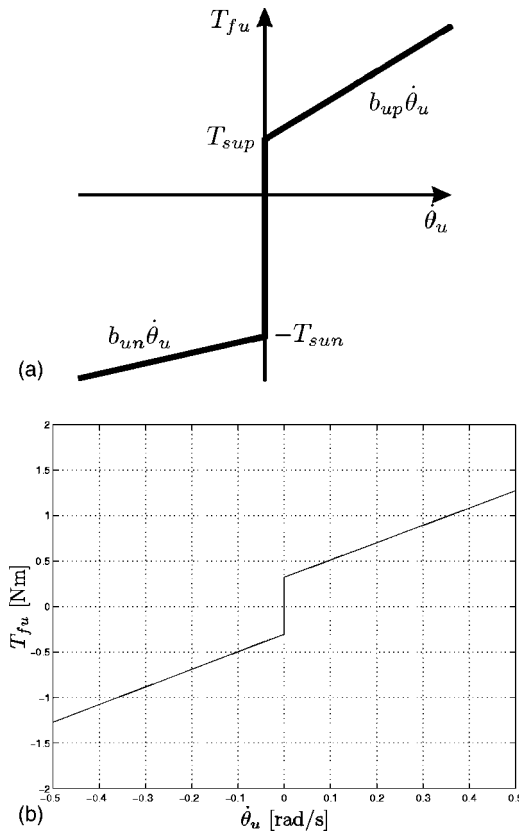


Fig. 2 Friction model at the upper disk

$$\dot{x}_2 = \frac{k_m}{J_u} u - \frac{k_\theta}{J_u} x_1 - \frac{1}{J_u} T_{fu}(x_2) \quad (10)$$

$$\dot{x}_3 = \frac{k_\theta}{J_l} x_1 - \frac{1}{J_l} T_{fl}(x_3)$$

This model is used for further analysis of the dynamic behavior of the drill-string setup.

2.3 Parameter Estimation and Friction Modeling. In order to obtain a predictive model of the drill-string setup, the parameters k_m , J_u , J_l , k_θ and nonlinear functions $T_{up}(\dot{\theta}_u)$, $T_{un}(\dot{\theta}_u)$, $T_{lp}(\dot{\theta}_l)$, and $T_{ln}(\dot{\theta}_l)$ need to be estimated.

First, in order to estimate the parameters concerning the upper part of the setup [k_m , J_u , and $T_{fu}(\dot{\theta}_u)$] the upper disk is disconnected from the lower disk. The parameter estimation is based on dedicated experiments involving responses of the system, when constant and white-noise input voltages u are applied, and an identification procedure ensuring a close match between the model predictions and experimental results (see, for example, [16]) and yields the following parameter values:

$$k_m = 3.5693 \frac{\text{Nm}}{\text{V}}, \quad J_u = 0.4765 \frac{\text{kg m}^2}{\text{rad}} \quad (11)$$

In order to determine friction torque T_{fu} , appropriate nonlinear functions $T_{up}(\dot{\theta}_u)$ and $T_{un}(\dot{\theta}_u)$ in (9) need to be determined. During the parameter estimation of the friction torque at the upper part of the setup, the following is noted:

- The Stribeck effect is not present in the friction torque at the upper disk. An explanation for this can be recognized in (6). Namely, this equation expresses that the friction in the bearings of the upper disk T_{fm} may very well be small with respect to the viscous friction term due to the electromagnetic forces in the DC motor. Experiments show that this is indeed the case. Therefore,

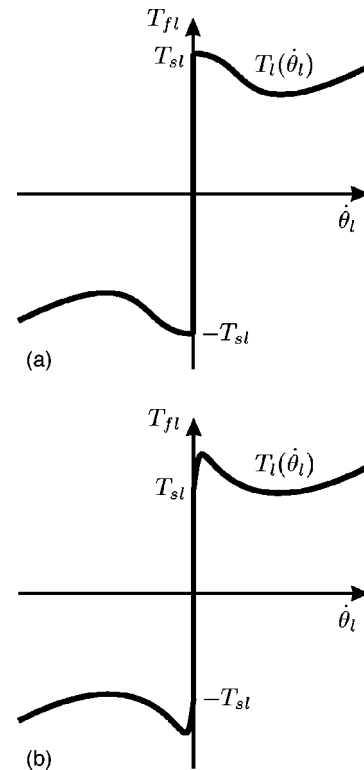


Fig. 3 Friction model at the lower disk

the friction torque at the upper disk T_{fu} is modeled as the Coulomb friction with the viscous friction as shown in Fig. 2(a).

• The friction torque at the upper disk is asymmetric. This means that $T_{fu}(\dot{\theta}_u) \neq -T_{fu}(-\dot{\theta}_u)$, i.e., $T_{up}(\dot{\theta}_u) \neq T_{un}(-\dot{\theta}_u)$.

Resuming, the friction torque at the upper part of the setup is modeled as

$$T_{fu}(\dot{\theta}_u) \in \begin{cases} T_{sup} + b_{up}\dot{\theta}_u & \text{for } \dot{\theta}_u > 0 \\ [-T_{sun}, T_{sup}] & \text{for } \dot{\theta}_u = 0 \\ -T_{sun} + b_{un}\dot{\theta}_u & \text{for } \dot{\theta}_u < 0 \end{cases} \quad (12)$$

with the following parameters:

$$\begin{aligned} T_{sup} &= 0.3216 \text{ Nm}, & T_{sun} &= 0.3026 \text{ Nm}, \\ b_{up} &= 1.9667 \frac{\text{kg m}^2}{\text{rad s}}, & b_{un} &= 2.0 \frac{\text{kg m}^2}{\text{rad s}} \end{aligned} \quad (13)$$

where b_{up} and b_{un} are equivalent viscous coefficients present at the upper disk for positive and negative angular velocities, respec-

tively, and T_{sup} and $-T_{sun}$ represent the maximum and minimum value of the friction torque for zero angular velocities. The estimated friction T_{fu} is shown in Fig. 2(b).

During the investigation of the steady-state behavior of the whole drill-string setup when no brake is applied at the lower disk, it is noted that for certain constant input voltages u , torsional vibrations appear. Moreover, those vibrations do *not* always exhibit the stick-slip phenomenon. In [1–5], it is stated that torsional vibrations in drill-string systems can be modeled using the friction model with the Stribeck effect [see Fig. 3(a)]. However, using such model, only torsional vibrations *with* stick-slip can be modeled. Therefore, a humped friction model [10,11], as shown in Fig. 3(b), is used. In Fig. 3, it can be seen that the difference between the humped friction model and the friction model with the Stribeck effect is evident for low angular velocities. Namely, in the humped friction model, positive damping is present for very small angular velocities which is not the case for the friction in Fig. 3(a).

Based on a neural network model [16–18], the friction torque in Fig. 3(b) can be expressed by

$$T_{fl}(\dot{\theta}_l) = \begin{cases} \left[T_{sl} + T_1 \left(1 - \frac{2}{1 + e^{\beta_1 |\dot{\theta}_l|}} \right) + T_2 \left(1 - \frac{2}{1 + e^{\beta_2 |\dot{\theta}_l|}} \right) \right] \text{sign}(\dot{\theta}_l) + b_l \dot{\theta}_l & \text{for } \dot{\theta}_l \neq 0, \\ [-T_{sl}, T_{sl}] & \text{for } \dot{\theta}_l = 0, \end{cases} \quad (14)$$

where T_{sl} , T_1 , T_2 , β_1 , β_2 , b_l are the parameters of the friction model. Moreover, T_{sl} represents the maximum static friction level, and b_l is the viscous friction coefficient.

Using dedicated experiments involving both transient and steady-state behavior of the setup and an identification procedure ensuring a close match between the experimental results and the corresponding model predictions, the remaining parameters of the setup (k_θ, J_l) and the parameters of the friction model (14) are obtained

$$J_l = 0.0326 \frac{\text{kg m}^2}{\text{rad}}, \quad k_\theta = 0.078 \frac{\text{Nm}}{\text{rad}} \quad (15)$$

$$\begin{aligned} T_{sl} &= 0.01663 \text{ Nm}, & b_l &= 0.00459 \frac{\text{kg m}^2}{\text{rad s}}, \\ T_1 &= 0.7016 \text{ Nm}, & T_2 &= -0.7173 \text{ Nm}, \end{aligned} \quad (16)$$

$$\beta_1 = 2.0427 \frac{\text{s}}{\text{rad}}, \quad \beta_2 = 1.9205 \frac{\text{s}}{\text{rad}}$$

The estimated friction torque is shown in Fig. 4(a).

A validation procedure is performed using different input signals such as quasi-random, harmonic, constant, ramp, and parabolic signals. For those signals, the comparison between the responses of the experimental setup and estimated model indicates the good quality of the obtained parameters.

In order to gain an improved insight in the causes for torsional vibrations in real drilling systems, an additional brake is applied to the lower disk of the experimental drill-string setup. The brake material is rubber. For several levels of the normal forces (see Fig. 5), no torsional vibrations in steady state are noted when a constant input voltage is applied. However, when water is added between the lower brass disk and the contact material of the brake, torsional steady-state vibrations appear for constant input voltages. Moreover, both torsional vibrations with and without stick-

slip behavior appear.² Therefore, this is a motivation for using friction model (14) for modeling the contact force between the brake and the lower disk. Due to the fact that we are interested in investigation of torsional vibrations of drill-string systems, we proceed with the analysis of the system when water is added in a reproducible fashion.

For the estimation of the parameters of the friction model (14) for the friction torque at the lower disk with brake, the estimated parameters (11) and (13) of system (10) are used. Next, a quasi-random signal is applied to the experimental setup. Then, using a nonlinear least-square technique we tried to ensure a close match between the experimentally obtained angular velocity $\dot{\theta}_l$ and the corresponding model prediction. In such a way, the following estimates for the parameters of the friction model (14) are obtained:

$$\begin{aligned} T_{sl} &= 0.0940 \text{ Nm}, & b_l &= 0.0042 \frac{\text{Nm}^2}{\text{rad s}}, & T_1 &= 0.0826 \text{ Nm}, \\ T_2 &= -0.2910 \text{ Nm} \\ \beta_1 &= 6.3598 \frac{\text{s}}{\text{rad}}, & \beta_2 &= 0.0786 \frac{\text{s}}{\text{rad}} \end{aligned} \quad (17)$$

The resulting estimated friction model at the lower disk with brake is shown in Fig. 4(b). A validation procedure for different input signals provides evidence for the good quality of the estimated model.

If we compare the estimated friction torque shown in Fig. 4(b) with the one shown in Fig. 4(a) and with the proposed friction torque [see Fig. 3(b)] it can be seen that the estimated friction torque, when the brake is applied at the lower disk, is qualitatively the same as the proposed model. However, in the friction torque in Fig. 4(b) the part observed for higher angular velocities, when viscous friction phenomenon is dominant, cannot be seen because:

²More about friction phenomenon due to a contact between two materials can be found in [12,13,19,20].

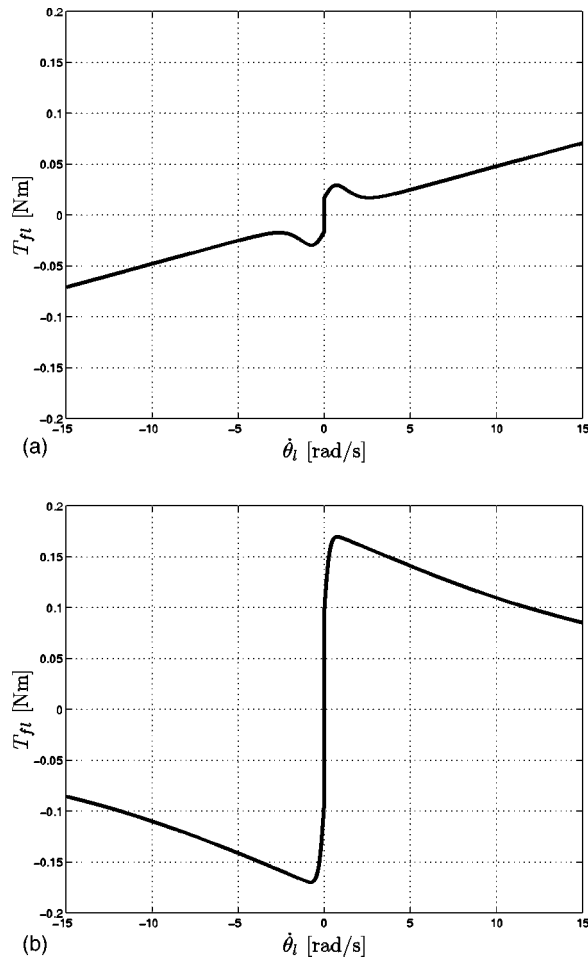


Fig. 4 Estimated friction torques at the lower disk

- The input voltage u , which is fed from the computer into the power amplifier of the motor, is limited ($u \in [-5 \text{ V}, 5 \text{ V}]$). Therefore, the maximal angular velocity, which can be achieved at both disks, is limited.
- During the parameter identification of the friction model at the lower disk, the maximally achieved angular velocity at the lower disk was around 12.6 rad/s.

Therefore, the estimated friction model for even higher velocities is less accurate. However, it is expected that for higher angular velocities the viscous friction phenomenon is dominant in the friction at the lower disk when the brake is applied.

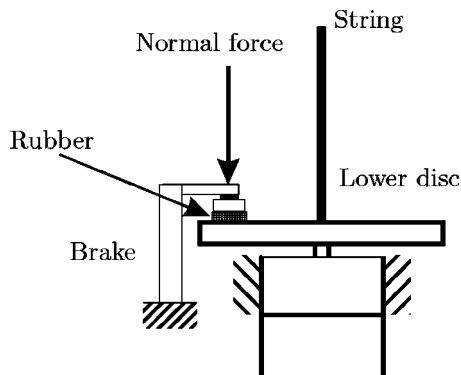


Fig. 5 Applied normal force at the brake of the lower disk

Since the steady-state behavior of the drill-string setup is of interest, in the sequel, such behavior of system (10), with the friction torque at the upper disk (12) and friction torque at the lower disk (14), is analyzed.

3 Analysis of Nonlinear Dynamic Behavior

Since both equilibria (constant velocity at both the upper and lower disk) and limit cycles (torsional vibrations at the lower disk) are observed in the experimental setup, in this section, both the equilibrium points (sets) and the limit cycles of the model as well as the related stability properties are analyzed.

3.1 Equilibrium Points. In the equilibrium points it holds that $(x_1, x_2, x_3) = (x_{1eq}, x_{2eq}, x_{3eq})$, for $u = u_c$, with u_c a constant, and $x_{1eq}, x_{2eq}, x_{3eq}$ satisfy the equations

$$\begin{aligned} x_{2eq} - x_{3eq} &= 0 \\ k_m u_c - T_{fu}(x_{3eq}) - T_{fl}(x_{3eq}) &= 0 \\ k_\theta x_{1eq} - T_{fl}(x_{3eq}) &= 0 \end{aligned} \quad (18)$$

From (18), it can be noted that the following two cases should be considered:

- equilibrium points for $x_{2eq} = x_{3eq} \neq 0$, i.e. both the lower and the upper disk rotate with the same constant angular velocity
- equilibrium points for $x_{2eq} = x_{3eq} = 0$, i.e. both the lower and the upper disk stand still

For $x_{3eq} > 0$, $T_{fu}(x_{3eq}) = T_{sup} + b_{up}x_{3eq}$ [see (12)] and $T_{fl}(x_{3eq}) = T_l(x_{3eq})$ with

$$\begin{aligned} T_l(x_{3eq}) &= T_{sl} + T_1 \left(1 - \frac{2}{1 + e^{\beta_1 |x_{3eq}|}} \right) + T_2 \left(1 - \frac{2}{1 + e^{\beta_2 |x_{3eq}|}} \right) \\ &\quad + b_l x_{3eq} \text{sign}(x_{3eq}) \end{aligned} \quad (19)$$

[see (14)]. Thus, such an equilibrium point should satisfy the following set of nonlinear algebraic equations:

$$\begin{aligned} x_{2eq} &= x_{3eq} \\ k_m u_c - b_{up} x_{3eq} - T_{sup} - T_l(x_{3eq}) &= 0 \\ x_{1eq} &= \frac{T_l(x_{3eq})}{k_\theta} \end{aligned} \quad (20)$$

From (4), (9), the second algebraic equation of (20) and due to the fact that $x_{3eq} > 0$, it can be concluded that the system only exhibits such an equilibrium point for $u_c > (T_{sup} + T_{sl})/k_m$. In general, the second equation in (20) can have more than one solution. For the estimated parameters (11), (13), and (15) of the system it holds that

$$-b_{up} - \frac{dT_l}{dx_3} < 0, \quad \forall x_3 > 0 \quad (21)$$

which means that the considered system has only one equilibrium point for given u_c for $x_{3eq} > 0$.

In a similar way, for $x_{3eq} < 0$, it follows that (10) has one equilibrium point that is a solution of

$$\begin{aligned} x_{2eq} &= x_{3eq} \\ k_m u_c - b_{un} x_{3eq} + T_{sun} + T_l(x_{3eq}) &= 0 \\ x_{1eq} &= -\frac{T_l(x_{3eq})}{k_\theta} \end{aligned} \quad (22)$$

with $u_c < -(T_{sun} + T_{sl})/k_m$.

In order to obtain local stability conditions for the equilibrium point for $x_{3eq} > 0$, the nonlinear system (10) is linearized around the equilibrium point for $u_c > (T_{sup} + T_{sl})/k_m$. According to the Routh-Hurwitz criterion, the equilibrium point of system (10) is locally asymptotically stable for

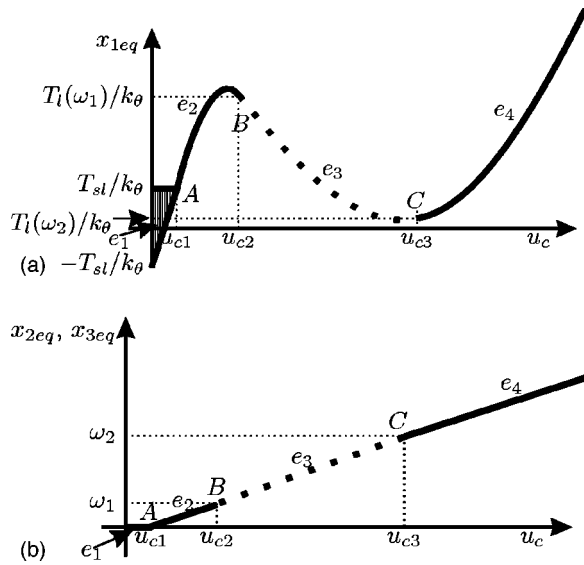


Fig. 6 Equilibrium branches of the drill-string setup

$$d_l > -0.00114 \frac{\text{kg m}}{\text{rad s}} \quad (23)$$

for the estimated system parameters (11), (13), and (15), with

$$d_l = \left. \frac{dT_l}{dx_3} \right|_{x_3=x_{3eq}} \quad (24)$$

where d_l represent the friction damping present at the lower disk when angular velocity is $\dot{\theta}_l = x_{3eq}$.

The same analysis can be performed for $u_c < -(T_{sl} + T_{sun})/k_m$ (the disk is rotating in negative direction), to obtain the local stability properties of the equilibrium points for $x_{3eq} < 0$.

The equilibrium points (set) for $x_{2eq} = x_{3eq} = 0$ exist only when the input voltage satisfies the condition

$$-\frac{T_{sun} + T_{sl}}{k_m} \leq u_c \leq \frac{T_{sup} + T_{sl}}{k_m} \quad (25)$$

From (18) it can be concluded that when (25) is satisfied, equilibrium points $\mathbf{x}_{eq} = (x_{1eq}, 0, 0)$ of the system are such that $\mathbf{x}_{eq} \in \mathcal{E}$, where \mathcal{E} represents the equilibrium set defined by

$$\mathcal{E} = \left\{ \mathbf{x} \in \mathbb{R}^3 \left| x_1 \in \left[\frac{-T_{sl}}{k_\theta}, \frac{T_{sl}}{k_\theta} \right] \cap \left[\frac{k_m u_c - T_{sup}}{k_\theta}, \frac{k_m u_c + T_{sun}}{k_\theta} \right], \right. \right. \\ \left. \left. x_2 = 0, x_3 = 0 \right\} \right. \quad (26)$$

Moreover, in the Appendix the stability properties of the equilibrium set (26) are discussed.

In Fig. 6 a sketch of the equilibrium branches for different constant input voltages u_c is plotted. Although we are interested in the behavior of the velocity of the lower disk for different constant input voltages [Fig. 6(b)], in Fig. 6(a) x_{1eq} ($x_1 = \theta_u - \theta_l$) for different u_c is shown. In Fig. 6 solid lines represent stable and dotted lines unstable equilibrium branches. If we use the results of the steady-state analysis of system (10) for $u = u_c \geq 0$ with u_c constant and take into account that the friction torque, present at the lower disk, is of the type shown in Fig. 3(b), then the following can be concluded:

- For $u_c \leq u_{c1}$, $u_{c1} = (T_{sup} + T_{sl})/k_m$ (point A in Fig. 6), the system is in the stick phase in steady state [see (25)], i.e. the system has locally asymptotically stable equilibrium set (see the

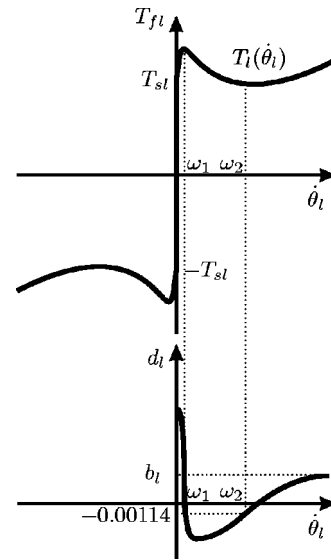


Fig. 7 Friction damping for suggested friction torque present at the lower disk of the drill-string setup

Appendix) described by (26) (equilibrium branch e_1 in Fig. 6). Namely, both the lower and the upper disks do not rotate (the equilibrium set satisfies $x_{2eq} = x_{3eq} = 0$) due to the fact that input voltage is not big enough to drive the upper and lower disks.

- The system has one equilibrium point for $u_c > u_{c1}$ [see (21)]. Given the fact that the friction torque at the lower disk is as shown in Fig. 3(b), it can be concluded that a stable equilibrium branch e_2 appears (see Fig. 6). Namely, for $u_c = u_{c1}$ the system leaves the stick phase, the steady-state velocity at the lower disk increases, the friction damping d_l of the friction torque at the lower disk is positive and starts to decrease (see Fig. 7). For a certain angular velocity $x_{3eq} = \omega_1$ (see Fig. 7), the friction damping $d_l = -0.00114 \text{ kg m/(rad s)}$ and the equilibrium point becomes unstable [see condition (23)]. From the second equation of (20) a corresponding $u_c = u_{c2}$ can be found for given $x_{3eq} = \omega_1$ (point B in Fig. 6). Therefore, for $u_{c1} < u_c < u_{c2}$ system has a locally asymptotically stable equilibrium point (equilibrium branch e_2 in Fig. 6).

- If u_c increases from $u_c = u_{c2}$, then the system has an unstable equilibrium point and the corresponding x_{3eq} increases as well. Next, for a certain value of x_{3eq} the friction damping d_l (which is negative) starts to increase and for $x_{3eq} = \omega_2$ (see Fig. 7), and for $u_c = u_{c3}$ (point C in Fig. 6), d_l reaches the value $d_l = -0.00114 \text{ kg m/(rad s)}$ and the equilibrium point becomes asymptotically stable again. Therefore, for $u_{c2} < u_c < u_{c3}$ the system has an unstable equilibrium point (equilibrium branch e_3 in Fig. 6).

- For $u > u_{c3}$, the system has a locally asymptotically stable equilibrium point (equilibrium branch e_4 in Fig. 6).

- For $u_c = u_{c1}$ (point A in Fig. 6) no change of stability properties occurs. Moreover, the locally asymptotically stable equilibrium set (26) becomes the locally asymptotically stable equilibrium point A.

- For $u_c = u_{c2}$ (point B in Fig. 6) and for $u_c = u_{c3}$ (point C in Fig. 6) a change in stability properties occurs. Namely, a pair of complex conjugate eigenvalues, related to the linearization of the nonlinear dynamics of (10) around the equilibrium point, cross the imaginary axis to the right-half complex plane. Therefore, Hopf bifurcations occur at these points.

3.2 Periodic Solutions. According to the previous analysis, Hopf bifurcation points occur for $u_c = u_{c2}$ and $u_c = u_{c3}$. Next, using a path-following technique in combination with a shooting method [21,22], limit cycles are computed numerically for the estimated model of the system. The results are shown in a bifurcation diagram in Fig. 8. In those figures, the maximal and mini-

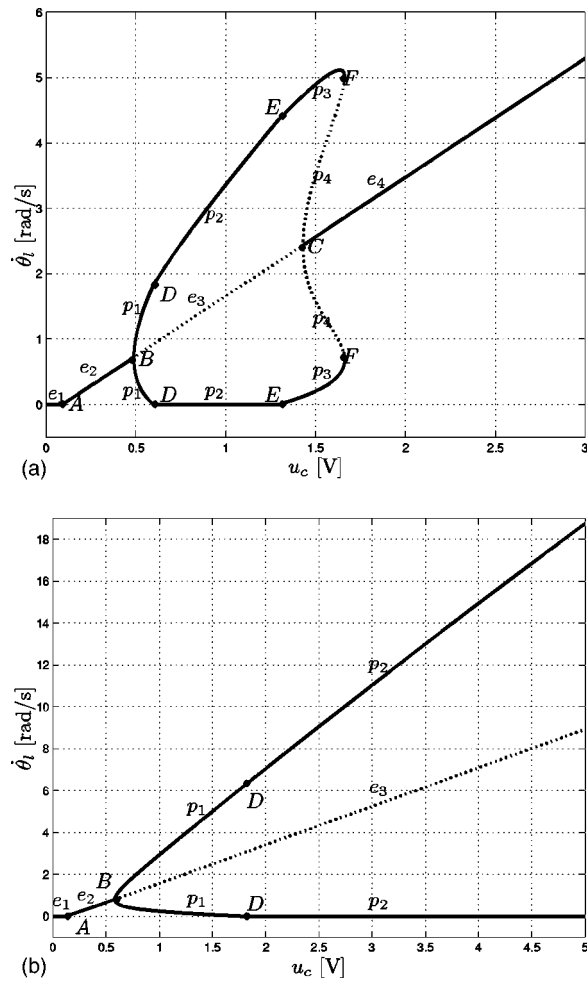


Fig. 8 Bifurcation diagrams of the drill-string setup

mal values of x_3 are plotted when a limit cycle is found. Floquet multipliers, corresponding to these limit cycles, are computed numerically and used to determine the local stability properties of these limit cycles. Since the estimated friction torque at the lower disk, when the brake is applied, is not considered to be accurate for higher angular velocities, where the viscous friction contribution is dominant, the obtained bifurcation diagram for corresponding higher input voltages is not determined. However, in order to understand the behavior of the setup for higher constant input voltages, the bifurcation diagram is constructed for the model of the system when no brake is applied. Then, the estimated friction torque at the lower disk [Fig. 4(a)] is of the form of the friction model in Fig. 3(b). The bifurcation diagram is shown in Fig. 8(a). With respect to the obtained results the following remarks can be made:

- From bifurcation point B for ($u_c > u_{c2}$), a locally unstable equilibrium branch e_3 arises (as discussed in the previous subsection) as well as a stable periodic branch p_1 . Therefore, point B represents a supercritical Hopf bifurcation point [23].
- Close to the bifurcation points, the periodic branch p_1 consists of limit-cycles which represent torsional vibrations without stick-slip. Therefore, bifurcation point B represents a smooth supercritical Hopf bifurcation point.
- At point D, torsional vibrations with stick-slip appear [branch p_2 in Fig. 8(a)], due to the nonsmooth nonlinearities in the friction torque at the lower disk. Moreover, the periodic branch p_2 is locally stable and point D does not represent a bifurcation point.

- For some higher constant input voltage u_c [point E in Fig. 8(a)] torsional vibrations without stick-slip appear once more (locally stable periodic branch p_3).
- Then, for even higher u_c , the locally stable periodic branch p_3 loses its stability and an unstable periodic branch appears [periodic branch p_4 in Fig. 8(a)]. The appearance of an unstable periodic solution in mechanical systems with a discontinuous friction force has already been analyzed in [3,24].
- The point where the stable periodic branch p_3 is connected to the unstable branch p_4 represents a fold bifurcation point [point F in Fig. 8(a)].
- The unstable periodic branch p_4 is connected to the equilibrium branches e_3 and e_4 in the Hopf bifurcation point C. Moreover, in Fig. 8(a) point C represents a subcritical Hopf bifurcation point.

For the model of the system when the brake is applied, the obtained bifurcation diagram is shown in Fig. 8(b). All equilibrium and periodic branches and bifurcation points, which are determined in the bifurcation diagram, appear in the bifurcation diagram of the system when no brake is applied. However, in the bifurcation diagram in Fig. 8(b), compared to the one shown in Fig. 8(a), the Hopf bifurcation point C, point E, fold bifurcation point F, equilibrium branch e_4 , and periodic branches p_3 and p_4 are not present. This is due to the fact that the maximal input voltage, which can be applied to the setup, is limited to 5 V. In Fig. 9, the limit cycles are depicted for $u = 1$ V, when no stick-slip is present, and for $u = 2$ V when stick-slip is present. Namely, in that figure the projection of those limit cycle on planes $x_1 = 0$ [Fig. 9(c)], $x_2 = 0$ [Fig. 9(b)], and $x_3 = 0$ [Fig. 9(a)] are shown.

4 Experimental Results

In order to check the validity of the obtained model of the drill-string setup when the brake is applied, experimental results are compared to the numerical results. As already mentioned, the evidence about the predictive quality of the estimated model in steady state is of great interest. Therefore, when a constant voltage is applied at the input of the setup, each experiment lasted long enough in order for all transient effects to disappear and the last 100 s of the angular velocity signal are recorded. Some of the obtained results are shown in Fig. 10. In this figure, the experimental angular velocity (solid line) and the angular velocity obtained using estimated model (dashed line) in steady state are shown for different constant input voltages. From the comparison between simulation and experimental results in Fig. 10, it can be concluded that with the suggested model the steady-state behavior of the setup is modeled accurately.

Next, the same type of bifurcation diagram, as shown in Fig. 8(b), is constructed experimentally. In order to construct such experimental bifurcation diagrams, different constant input voltages are applied to the setup. When no torsional vibrations are observed [as in Fig. 10(a)], the mean value of the recorded angular velocity is computed. Next, when torsional vibrations are observed at the lower disk [as in Figs. 10(b)–10(d)], the mean value of local maxima and minima are computed as well. Then, all experimentally obtained data for constant input voltages are plotted using the symbol o in Fig. 11. Such experimental results, together with the bifurcation diagram obtained by numerical analysis of the estimated model, are shown in Fig. 11(a). Moreover, when torsional vibrations are observed in the setup, the period time T of the vibrations is determined as well. In Fig. 11(b) such experimental results are compared to the period time of the numerically obtained limit cycles. The results shown in Fig. 11 illustrate the predictive quality of the obtained model.

Therefore, according to Figs. 11(a) and 11(b) it can be concluded that the observed torsional vibrations are caused by the nonlinearity present in the friction at the lower disk and such nonlinearity is modeled adequately using the friction model shown in Fig. 3(b). Figure 11 shows that the amplitude of the vibrations depends on the applied constant input voltage while the

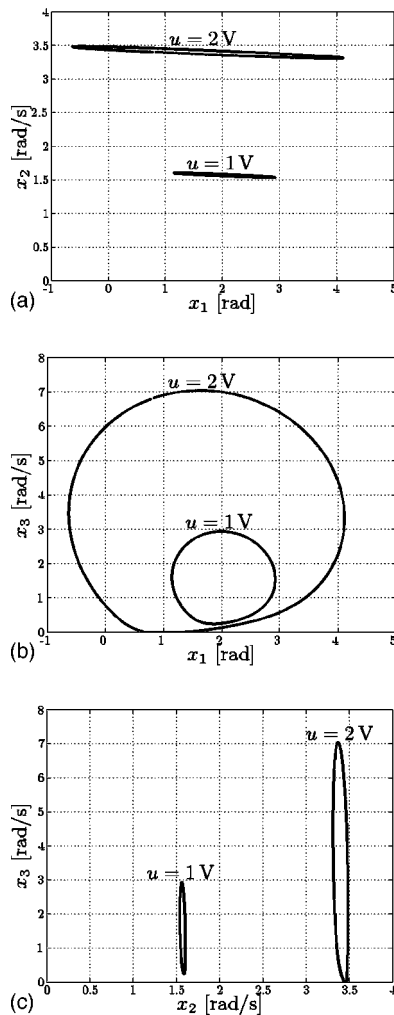


Fig. 9 Two types of limit cycles in state-space: for $u=1$ V (no stick-slip is present) and for $u=2$ V (stick-slip is present). $x_1 = \theta_u - \theta_l$, $x_2 = \dot{\theta}_u$, $x_3 = \dot{\theta}_l$.

period time shows only small changes. Moreover, it can be seen that the period time of the observed vibrations is very close to the period time of the linear resonance frequency T_r of the setup ($T_r = 0.045$ s).

4.1 Hopf Bifurcation Point. Both from the analysis of the estimated model and from the experimental results, it can be concluded that a supercritical Hopf bifurcation point [point B in Fig. 11(a)] exists. In the sequel, the experimental results, during the transition between the stable equilibrium branch [e_2 in Fig. 11(a)] and the locally stable periodic branch [p_1 in Fig. 11(a)], are analyzed.

From the results, shown in Figs. 10 and 11(a), it is concluded that for constant input voltage $u=0.5$ V no torsional vibrations are present, while for $u=1.0$ V vibrations are present in the system. In Fig. 12, experimentally obtained angular velocities of the lower disk are shown during the transition along the supercritical Hopf bifurcation point. From this figure, it can be concluded that some unmodeled behavior is present in the setup. In order to gain improved insight into the behavior of the system in steady state around the Hopf bifurcation point, the power spectral density of the experimentally obtained angular velocities is constructed and shown in Fig. 13. The resolution of the power spectrum is 0.01 Hz and its frequency range is 500 Hz. In Fig. 13, the power spectral density of the obtained signals is shown up to the frequency of 2 Hz, because for higher frequencies it drops to even lower values.

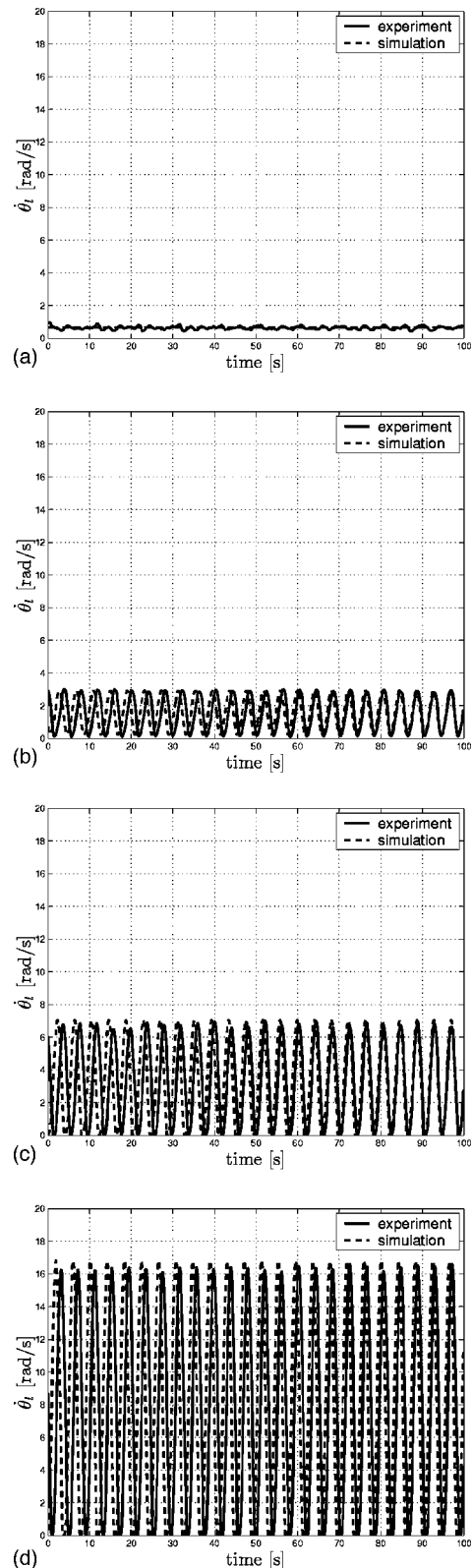


Fig. 10 Experimental and simulated angular velocity response of the lower disk in steady state for different constant input voltages when the brake is applied

Analyzing the results in Figs. 12 and 13, the following should be noted:

- For $u=0.2$ V, in Fig. 12(a) some low frequency vibrations

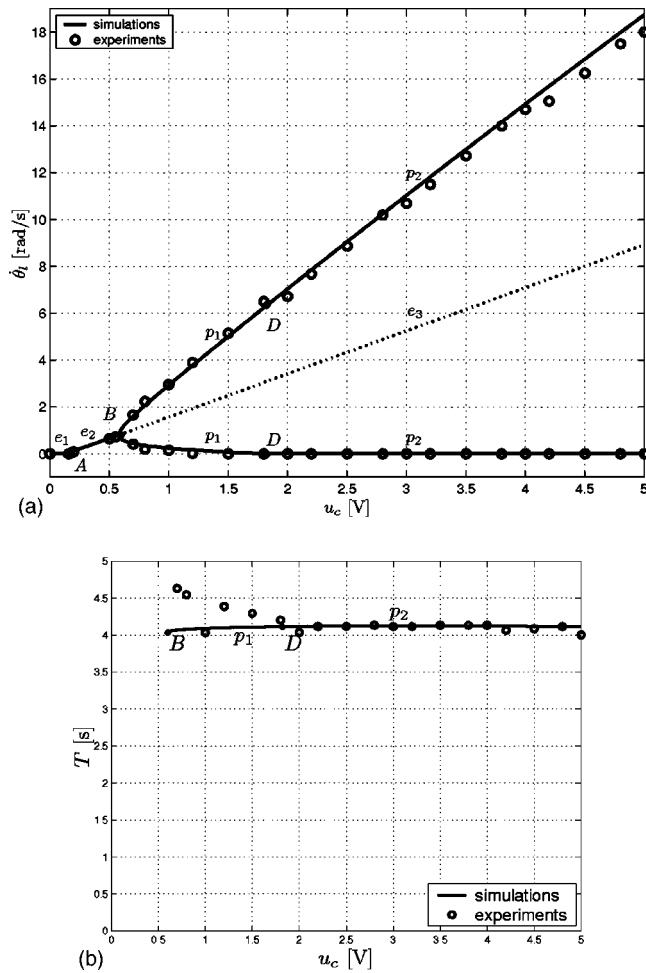


Fig. 11 Simulated and experimental results (circles) of the steady-state analysis of the drill-string setup

can be recognized. The mean value of experimentally obtained angular velocity is $\dot{\theta}_{lmean} = 0.0911 \text{ rad/s} = 0.0145 \text{ Hz}$. Comparing this result to the period time of the signal in Fig. 12(a) can lead to the conclusion that position-dependent friction, which is not modeled, is present in the system (i.e., that the friction at the lower disk is not the same at each angular position of the disc). Moreover, the same conclusion can be derived from the corresponding power spectral density signal shown in Fig. 13(a). Namely, some very low frequency vibrations in a frequency range between 0.01 Hz and 0.02 Hz can be recognized in the system. However, apart from position-dependent friction, also other unmodeled behavior is present in the recorded results, such as measurement noise, unmodeled friction dynamics, noise due to the fact that the angular velocity is obtained numerically, etc.

- For $u = 0.5 \text{ V}$, some torsional vibrations can be noted that do not have a regular period time and amplitude compared to the results shown for $u = 1.0 \text{ V}$ [Fig. 10(b)], $u = 2.0 \text{ V}$ [Fig. 10(c)] and $u = 4.5 \text{ V}$ [Fig. 10(d)]. This leads to the conclusion that the cause for those vibrations does not have the same nature as the cause for vibrations shown in Figs. 10(b)–10(d). If we analyze the power spectrum of the angular velocity [see Fig. 13(b)], it can be noted that the spectral content is considerably higher than the one shown in Fig. 13(a). Moreover, it can also be noted that some important spectral components are present at the frequencies that are a multiple of $f = 0.10 \text{ Hz}$. If we take into account that the mean value of the experimentally obtained angular velocity [shown in Fig.

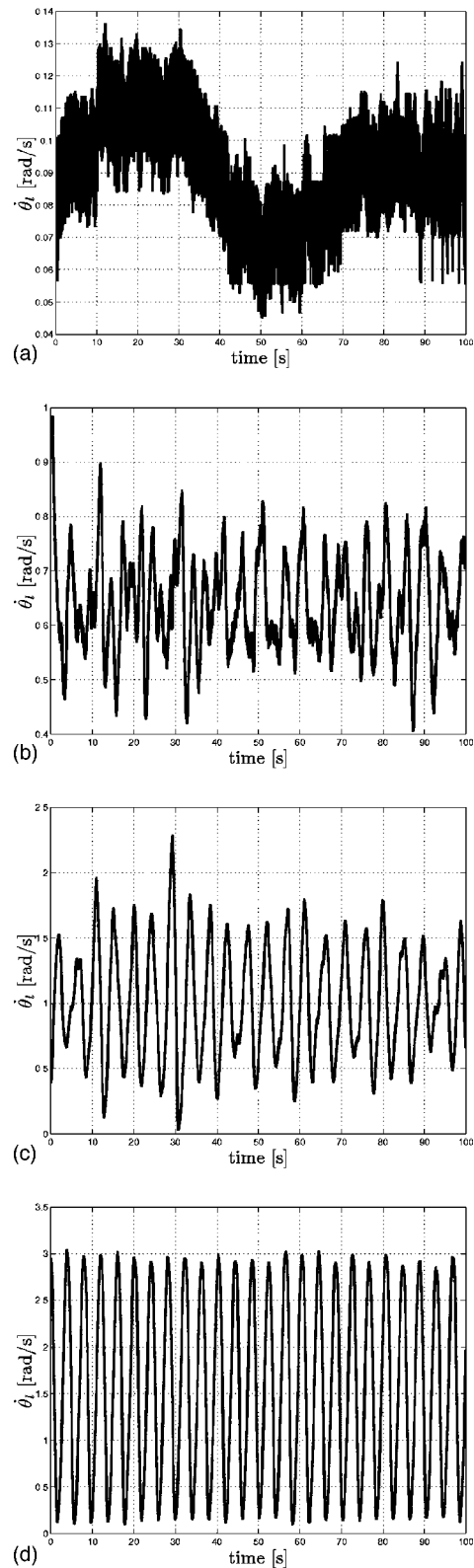


Fig. 12 Angular velocity of the lower disk in steady state for different constant input voltages when the brake is applied

12(b)] is $\dot{\theta}_{lmean} = 0.6411 \text{ rad/s} = 0.1020 \text{ Hz}$, this can represent more evidence of the presence of the position-dependent friction at the lower disk.

- For $u = 0.7 \text{ V}$ the torsional vibrations [shown in Fig. 12(c)] have a more regular period time although the amplitude of the

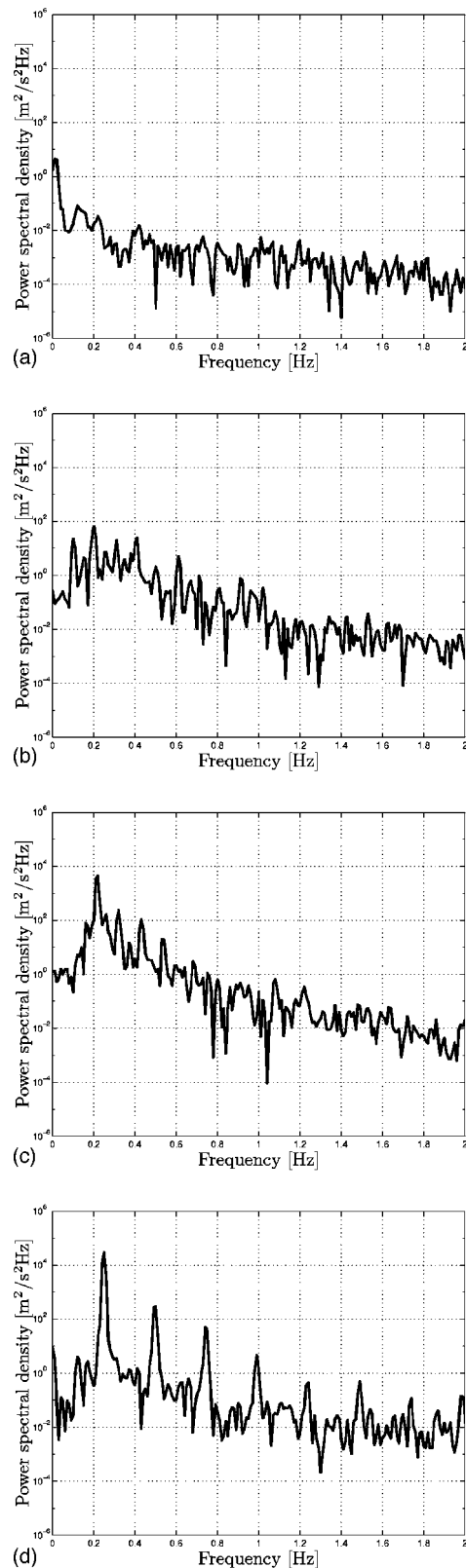


Fig. 13 Power spectral density of the angular velocities shown in Fig. 12

vibrations varies significantly. In the power spectrum shown in Fig. 13(c), a dominant spectral component at a frequency between 0.21 Hz and 0.22 Hz appears. The observed period time is close to that observed for the estimated model [see Fig. 11(b)] and has no

connection with the mean value of the angular velocity of the lower disk ($\dot{\theta}_{mean} = 1.0077 \text{ rad/s} = 0.1604 \text{ Hz}$). Therefore, the main cause for such a torsional vibration is the nonlinearity in the friction torque, which is modeled as shown in Fig. 3(b) and analyzed in the previous section. The fact that the amplitude of the observed vibrations significantly varies can be due to the large influence of the observed unmodeled behavior of the setup. However, this signal is considered to be a limit cycle caused by nonlinear friction torque (14).

- For $u = 1.0 \text{ V}$, torsional vibrations in the velocity at the lower disk exhibit a regular period time. The amplitude of the vibrations is reasonably constant, which is evident from Fig. 12(d). In Fig. 13(d) a dominant spectral component at the frequency of 0.25 Hz can be noted, but also the higher harmonic components at the frequencies that are multiples of this dominant frequency component are observed. The existence of higher harmonics is an indication that the torsional vibrations are caused by the nonlinearity in the system. Therefore, this signal is also recognized as a limit cycle.

This performed analysis allows us to estimate the Hopf bifurcation point in the considered setup experimentally and to gain improved understanding of the behavior of the system around the Hopf bifurcation point.

5 Conclusions

In this paper, the steady-state behavior of a drill-string setup is analyzed when torsional vibrations appear. First, the dynamic model of the setup is introduced and the parameters of the setup are estimated. In the setup, when no brake is applied at the lower disk, torsional vibrations in steady state with and without stick-slip are observed. Torsional stick-slip vibrations in drill-string systems can be predicted using a static friction model with the Stribeck effect [1–5,7]. However, torsional vibrations without stick-slip cannot be modeled using the same friction model. Therefore, a humped discontinuous static friction model [10–13] is used. The difference between the humped friction model and a friction model with only the Stribeck effect is that for very small angular velocities the proposed friction model has a positive damping. With such a model, the observed torsional vibrations in the experimental setup, both with and without stick-slip, are successfully predicted.

Next, in order to gain insight into the causes for torsional vibrations in drill-string systems, an additional brake is applied at the lower disk. It is noted that no torsional vibrations appear until water has been added between the contact materials of the brake and the disk. When water is added torsional vibrations with and without stick-slip are observed. Subsequently, the parameters of the suggested model for the friction torque, present at the lower disk, are estimated and a steady-state analysis for the estimated model of the setup is performed. As a result of the steady-state analysis, a bifurcation diagram, with constant input voltage u_c as a bifurcation parameter, is presented. Moreover, a comparison between the numerical and experimental bifurcation diagrams illustrates the predictive quality of the suggested model.

As a result of the analysis and the obtained bifurcation diagrams, the following can be concluded:

- For very small constant input voltages, the lower disk cannot move. Namely, such small voltages cannot drive the motor of the setup because the sticking phenomenon is present in the friction at both the upper and lower disks. This effect is successfully modeled using discontinuous friction models.
- For higher constant input voltages, the upper and lower disks start to move and no torsional vibrations are present at the lower disk in steady state. When the constant input voltage is increased, at a certain level torsional vibrations without stick-slip appear at the lower disk. Moreover, for even higher levels of the constant input voltage the amplitude of the vibrations becomes higher and the torsional stick-slip vibrations appear.

• If the input voltage is high enough, based on the results when the brake is not applied, it is expected that the torsional vibrations disappear. This is due to the fact that at higher angular velocities the viscous friction becomes dominant in the friction at the lower disk. This effect is not observed in the setup when the brake is applied because the input voltage, which can be applied to the setup, is limited and the torsional deformations of the string may become too high for such high input voltage.

When analyzing the behavior of the setup in the vicinity of the supercritical Hopf bifurcation point, it is noted that not only the negative damping in the friction force at the lower disk is the cause for torsional vibrations. Namely, it has been observed that the friction force present in the setup is position dependent. Such a friction feature is not captured by the model. However, this can also cause the appearance of torsional vibrations. The period time of the vibrations caused by position-dependent friction characteristic depends on the angular velocity of the disk. In the considered setup, such vibrations were dominant until torsional vibrations caused by the (modeled) nonlinearity in the friction appeared. The latter type of vibrations exhibits a period time that is not related to the angular velocity of the lower disk and is close to the period time of the mechanical resonance.

Appendix: Local Asymptotic Stability of Equilibrium Set \mathcal{E}

When condition (25) is satisfied, it is concluded that system (10) exhibits an equilibrium set \mathcal{E} , given by (26), with u_c constant. In order to prove the local asymptotic stability of the equilibrium set \mathcal{E} , first it will be proven that \mathcal{E} is stable in the sense of Lyapunov and, next, using LaSalle's invariance principle, it will be proven that the equilibrium set is locally attractive. Moreover, a region of attraction will be estimated. Finally, combining the fact that \mathcal{E} is stable and locally attractive leads us to the conclusion that the equilibrium set is locally asymptotically stable.

In order to prove the stability of the equilibrium set, the following Lyapunov candidate function is considered:

$$V(\mathbf{x}, \mathbf{x}_{eq}) = \frac{1}{2}k_\theta(x_1 - x_{1eq})^2 + \frac{1}{2}J_u x_2^2 + \frac{1}{2}J_l x_3^2 \quad (27)$$

where $\mathbf{x}_{eq} = (x_{1eq}, 0, 0) \in \mathcal{E}$. According to (10), the time derivative of V obeys

$$\dot{V}(\mathbf{x}, \mathbf{x}_{eq}) = x_2[k_m u_c - k_\theta x_{1eq} - T_{fu}(x_2)] + x_3[k_\theta x_{1eq} - T_{fl}(x_3)]. \quad (28)$$

Due to the fact that the friction torque at the upper disc T_{fu} is estimated as shown in (12), it follows that

$$x_2[k_m u_c - k_\theta x_{1eq} - T_{fu}(x_2)] \leq 0 \quad (29)$$

for every $\mathbf{x} \in \mathbb{R}^3$. Next, knowing that $T_l(13 \text{ rad/s}) = T_{sl}$ [see Fig. 4(b)] it can be seen that for the estimated friction torque at the lower disk, it holds that $|T_l(x_3)| > T_{sl}$ for $|x_3| < 13 \text{ rad/s}$. Therefore, for every $\mathbf{x}_{eq} \in \mathcal{E}$ and $\mathbf{x} \in \mathcal{B}$, with

$$\mathcal{B} = \{\mathbf{x} \in \mathbb{R}^3 \mid |x_3| < 13 \text{ rad/s}\} \quad (30)$$

it holds that

$$x_3[k_\theta x_{1eq} - T_{fl}(x_3)] \leq 0 \quad (31)$$

and consequently, $\dot{V} \leq 0$. Therefore, each equilibrium point in \mathcal{E} is stable in the sense of Lyapunov.

Next, in order to prove that the equilibrium set \mathcal{E} is stable in the sense of Lyapunov, sets \mathcal{A}_δ , \mathcal{A}_ϵ , and \mathcal{S} are introduced

$$\begin{aligned} \mathcal{A}_a &= \{\mathbf{x} \in \mathbb{R}^2 \mid \|\mathbf{x} - \text{prox}_{\mathcal{E}}(\mathbf{x})\| \leq a\}, \\ \text{prox}_{\mathcal{E}}(\mathbf{x}) &= \arg\min_{\mathbf{x}^* \in \mathcal{E}} \|\mathbf{x} - \mathbf{x}^*\|, \quad a \in \{\delta, \epsilon\} \\ \mathcal{S} &= \bigcup_{\mathbf{x}_{eq} \in \mathcal{E}} \mathcal{S}_{\mathbf{x}_{eq}}, \quad \mathcal{S}_{\mathbf{x}_{eq}} = \{\mathbf{x} \in \mathbb{R}^3 \mid V(\mathbf{x}, \mathbf{x}_{eq}) < r\}. \end{aligned} \quad (32)$$

According to the previous analysis, it can be seen that for all $\epsilon > 0$, we can choose r such that $r < c$, with $c = J_l 13^2/2$, and $\mathcal{S} \subset \mathcal{A}_\epsilon$. Then, for the chosen \mathcal{S} (and r), δ can be chosen such that $\mathcal{A}_\delta \subset \mathcal{S}$. Consequently, for every $t_0 \geq 0$ it follows that

$$\mathbf{x}(t_0) \in \mathcal{A}_\delta \Rightarrow \mathbf{x}(t) \in \mathcal{A}_\epsilon \forall t \geq t_0 \quad (33)$$

Namely, for every $r < c$ it holds that $\mathcal{A}_\delta \subset \mathcal{S} \subset \mathcal{B}$. Consequently, $\dot{V}(\mathbf{x}, \mathbf{x}_{eq}) \leq 0$ and, therefore, the equilibrium set \mathcal{E} is stable in the Lyapunov sense.

Let us now show that the equilibrium set \mathcal{E} is locally attractive. For that purpose, let $V_1(\mathbf{x}) = V(\mathbf{x}, \mathbf{0})$ and define the set \mathcal{C} by

$$\mathcal{C} = \{\mathbf{x} \in \mathbb{R}^3 \mid V_1(\mathbf{x}) \leq c\} \quad (34)$$

Then, the previous analysis yields $\dot{V}_1 \leq 0$ for all $\mathbf{x} \in \mathcal{C}$. Next, for the estimated friction torques $T_{fu}(x_2)$ and $T_{fl}(x_3)$, from (28) it can be concluded that $\dot{V}_1 = 0$ for $\mathbf{x} \in \mathcal{L}$, with

$$\mathcal{L} = \{\mathbf{x} \in \mathbb{R}^3 \mid x_2 = 0, x_3 = 0\} \quad (35)$$

Consider the vector field $\mathbf{f}(\mathbf{x}(t), u_c)$, given by

$$\mathbf{f}(\mathbf{x}(t), u_c) = \begin{bmatrix} x_2 - x_3 \\ \frac{k_m}{J_u} u_c - \frac{k_\theta}{J_u} x_1 - \frac{1}{J_u} T_{fu}(x_2) \\ \frac{k_\theta}{J_l} x_1 - \frac{1}{J_l} T_{fl}(x_3) \end{bmatrix} \quad (36)$$

[see the equations of the system (10)]. Then, $\mathbf{f}(\mathbf{x}(t), u_c)$ on the set \mathcal{L} , is such that $\mathbf{f}(\mathbf{x}(t), u_c) = \mathbf{f}_l(\mathbf{x}(t), u_c)$, with

$$\mathbf{f}_l(\mathbf{x}(t), u_c) = \begin{bmatrix} 0 \\ \frac{k_m}{J_u} u_c - \frac{k_\theta}{J_u} x_1 - \frac{1}{J_u} T_{fu}(0) \\ \frac{k_\theta}{J_l} x_1 - \frac{1}{J_l} T_{fl}(0) \end{bmatrix} \quad (37)$$

When the upper disk is in stick ($x_2 = 0$) then $\dot{x}_2 = 0$ and $T_{fu}(x_2) = T_{fu}(0) \in [-T_{sun}, T_{sup}]$ [see (12)]. Consequently, it holds that $x_1 \in [(k_m u_c - T_{sup})/k_\theta, (k_m u_c + T_{sun})/k_\theta]$. Similarly, when the lower disk is in stick phase ($x_3 = 0$), then $\dot{x}_3 = 0$, $T_{fl}(x_3) = T_{fl}(0) \in [-T_{sl}, T_{sl}]$ [see (14)] and consequently $x_1 \in [T_{sl}/k_\theta, T_{sl}/k_\theta]$. Therefore, for every $\mathbf{x} \in \mathcal{L}$, which is not in \mathcal{E} either the second or third component of $\mathbf{f}_l(\mathbf{x}(t), u_c)$ is always non-zero. This leads us to the conclusion that the equilibrium set \mathcal{E} represents the largest invariant set on \mathcal{L} when condition (25) is satisfied.

Moreover, it can be shown that only attractive sliding modes or transversal intersections can occur at the switching surfaces Σ_1 and Σ_2 with

$$\Sigma_1 = \{\mathbf{x} \in \mathbb{R}^3 \mid x_2 = 0\}, \quad \Sigma_2 = \{\mathbf{x} \in \mathbb{R}^3 \mid x_3 = 0\} \quad (38)$$

and that repulsive sliding modes are not present. Uniqueness of solutions is, therefore, guaranteed [3], which could also be inferred from the fact that the set-valued friction laws (9) and (14) take values in minimal closed convex sets for zero relative velocity and are always dissipative.

The application of LaSalle's invariance principle [23,25] now proves that equilibrium set \mathcal{E} is locally attractive. Moreover, the set \mathcal{C} represents an estimate for the region of attraction. Finally, since we proved that the equilibrium set \mathcal{E} is stable and locally attractive, then we can conclude that \mathcal{E} is locally asymptotically stable.

References

- [1] Jansen, J. D., 1993, "Nonlinear Dynamics of Oil-Well Drill-Strings," Ph.D. thesis, Delft University Press, The Netherlands.
- [2] Jansen, J. D., and van de Steen, L., 1995, "Active Damping of Self-Excited Torsional Vibrations in Oil Well Drillstrings," *J. Sound Vib.*, **179**(4), pp. 647–668.
- [3] Leine, R. I., 2000, "Bifurcations in Discontinuous Mechanical Systems of

- Filippov-Type," Ph.D. thesis, Eindhoven University of Technology, Eindhoven, The Netherlands.
- [4] Leine, R. I., van Campen, D. H., and Keultjes, W. J. G., 2002, "Stick-Slip Whirl Interaction in Drillstring Dynamics," *ASME J. Vibr. Acoust.*, **124**, pp. 209–220.
 - [5] Van den Steen, L., 1997, "Suppressing Stick-Slip-Induced Drill-String Oscillations: A Hyper Stability Approach," Ph.D. thesis, University of Twente, Enschede, The Netherlands.
 - [6] Brett, J. F., 1992, "The Genesis of Torsional Drillstring Vibrations," *SPEDE*, **7**(3), pp. 168–174.
 - [7] Kust, O., 1998, "Selbsterregte Drehschwingungen in Schlanken Torsionssträngen: Nichtlineare Dynamik und Regelung," Ph.D. thesis, Technincal University Hamburg-Harburg, Germany.
 - [8] Cunningham, R. A., 1968, "Analysis of Downhole Measurements of Drill String Forces and Motions," *ASME J. Eng. Ind.*, **90**, pp. 208–216.
 - [9] Tucker, R. W., and Wang, C., 1999, "An Integrated Model for Drill-String Dynamics," *J. Sound Vib.*, **224**(1), pp. 123–165.
 - [10] Brockley, C. A., Cameron, R., and Potter, A. F., 1967, "Friction-Induced Vibration," *ASME J. Lubr. Technol.*, **89**, pp. 101–108.
 - [11] Brockley, C. A., and Ko, P. L., 1970, "Quasi-Harmonic Friction-Induced Vibration," *ASME J. Lubr. Technol.*, **92**, pp. 550–556.
 - [12] Ibrahim, R. A., 1994, "Friction-Induced Vibration, Chatter, Squeal, and Chaos; Part I: Mechanics of Contact and Friction," *Appl. Mech. Rev.*, **47**(7), pp. 209–226.
 - [13] Ibrahim, R. A., 1994, "Friction-Induced Vibration, Chatter, Squeal, and Chaos; Part II: Dynamics and Modeling," *Appl. Mech. Rev.*, **47**(7), pp. 227–253.
 - [14] Krauter, A. I., 1981, "Generation of Squeal/Chatter in Water-Lubricated Elastomeric Bearings," *ASME J. Lubr. Technol.*, **103**, pp. 406–413.
 - [15] Leonard, W., 2001, *Control of Electrical Drives*, Springer-Verlag, Berlin.
 - [16] Hensen, R. H. A., 2002, *Controlled Mechanical Systems with Friction*, Ph.D. thesis, Eindhoven University of Technology, Eindhoven, The Netherlands.
 - [17] Hensen, R. H. A., Angelis, G. Z., Molengraft v. d., M. J. G., Jager d., A. G., and Kok, J. J., 2000, "Gray-Box Modeling of Friction: An Experimental Case-Study," *Eur. J. Control*, **6**(3), pp. 258–267.
 - [18] Narendra, K. S., and Parthasarathy, K., 1990, "Identification and Control of Dynamical Systems Using Neural Networks," *IEEE Trans. Neural Netw.*, **1**, pp. 4–27.
 - [19] Armstrong-Hélouvry, B., and Amin, B., 1994, "A Survey of Models, Analysis Tools and Compensation Methods for the Control of Machines With Friction," *Automatica*, **30**(7), pp. 1083–1138.
 - [20] Leonov, A. I., 1990, "On the Dependence of Friction Force on Sliding Velocity in the Theory of Adhesive Friction of Elastomers," *Wear*, **141**, pp. 137–145.
 - [21] Ascher, U. M., Mattheij, R. M. M., and Russell, D. R., *Numerical Solution of Boundary Value Problems for Ordinary Differential Equations*, SIAM, Philadelphia, 1995.
 - [22] Parker, T. S., and Chua, L. O., 1989, *Practical Numerical Algorithms for Chaotic Systems*, Springer-Verlag, Berlin.
 - [23] Sastry, S., 1999, *Nonlinear Systems*, Springer-Verlag, New York.
 - [24] Leine, R. I., and van Campen, D. H., 2004, "Discontinuous Fold Bifurcations," *Syst. Anal. Model. Simul.*, **43**(3), pp. 321–332.
 - [25] Van de Wouw, N., and Leine, R. I., 2004, "Attractivity of Equilibrium Sets of Systems With Dry Friction," *Nonlinear Dyn.*, **35**, pp. 19–39.